Concerted localization resets precede YAP-dependent transcription

*****J. Matthew Franklin[1-5], ***** [#]Rajarshi P. Ghosh[1-4], Quanming Shi[1-4], [#]Jan T. Liphardt[1-4]

[1] Bioengineering, Stanford University, Stanford, CA 94305, USA
[2] BioX Institute, Stanford University, Stanford, CA 94305, USA
[3] ChEM-H, Stanford University, Stanford, CA 94305, USA
[4] Cell Biology Division, Stanford Cancer Institute, Stanford, CA 94305, USA
[5] Chemical Engineering, Stanford University, Stanford, CA 94305, USA

***** Authors contributed equally.
[#] Correspondence and requests for materials should be addressed to rajarshi@stanford.edu or jan.liphardt@stanford.edu

Yes-associated protein 1 (YAP) is a transcriptional regulator with critical roles in mechanotransduction, organ size control, and regeneration. Here, we report a robust experimental platform for real-time visualization of native YAP dynamics and target gene expression. Using this platform, we show that activation of YAP target genes is preceded by concerted localization resets, which are dramatic, concerted departure/reentry cycles of nuclear YAP. These resets could be induced by calcium signaling, acto-myosin contractility, and mitotic-exit, and were strictly correlated with YAP-dependent transcription measured using nascent-transcription reporter knockins of YAP target genes. Oncogenically transformed cells with chronically elevated YAP-driven transcription lacked resets but rapidly exchanged YAP between the nucleus and cytoplasm, suggesting an escape from compartmentalization-based control. The single-cell YAP localization and transcription traces suggest a new mode of transcriptional regulation involving the concerted re-partitioning of YAP prior to gene activation.

Results and Discussion

The YAP (YES-associated protein) / TAZ (transcriptional coactivator with PDZ-binding motif) duo(*1*), a central node of the Hippo pathway (*2*)(*3*), controls organ size, and is critical for mechanotransduction (*4*)(*5*)(*6*). The classic view of YAP signal transduction equates nuclear enrichment with activation of pro-growth transcriptional programs through association with the TEAD family of transcription factors (*7*) (*8*) (*9*). However, other critical signal transducers such as ERK, NfkB and P53 use a rich signal transmission code in which the amplitude, frequency, and duration of their nucleocytoplasmic shuttling all influence gene transcription(*10*)(*11*)(*12*). Given recent reports that both YAP and TEAD can alter subcellular localization(*13*)(*14*)(*15*)(*16*), we speculated that their subcellular spatiotemporal dynamics may encode upstream signaling information. More generally, we should not expect biological signal transmission circuits to be simple, e.g. a linear mapping between an external input onto downstream gene expression level. There are now many examples of gene circuits with hysteresis, memory, and latching(*17*)(*18*)(*19*)(*20*)(*21*). Since these circuits involve spatially-controlled components such as transcription factors, it is natural to wonder about the interplay of cellular spatial dynamics and signal processing.

To investigate these ideas, we sought to quantify the localization dynamics of native YAP/TEAD in single cells and relate such dynamics to downstream transcription. We used CRISPR(*22*) to fluorescently tag native YAP and TEAD in breast epithelial cell lines commonly used for studying *hippo* signaling(*23*) (Methods, Figure 1a). Since transcription is pulsatile(*24*)(*25*), relating localization dynamics to target gene activity requires real-time measurement of gene transcription. We therefore used CRISPR to tag the native mRNAs of two classic YAP/TEAD targets, ANKRD1 (*26*) and AREG (*27*), with 24x-MS2 transcriptional reporters.

A recent report has shown that like YAP, TEAD undergoes cytoplasmic sequestration in HEK 293T cells at high cell densities (*16*). To simultaneously track YAP and TEAD subcellular localization in real time, we generated a dual CRISPR knockin MCF10A cell line where native YAP and TEAD1 (the most abundant TEAD family member in MCF10A)(*28*) were genomically tagged with eGFP and mCherry respectively (Methods, Figure 1b). Indeed, while YAP showed significant cytoplasmic sequestration, TEAD1 localization remained nuclear (Figure 1c). In the remainder of the study, we therefore focused on YAP.

Simultaneous tracking of local cell density and YAP localization revealed that MCF10A$^{\text{YAP-GFP-KI}}$ monolayers maintain constant YAP N/C up to a local density threshold, after which N/C decreases with a concomitant increase in local cell density (Figure 1d, Supplementary Movie 1). At low density, newly divided cells maintained constant local cell density by migrating to void-spaces. Further division cycles depleted the voids, packing the cells and driving cytoplasmic sequestration of YAP.

Since HRas transformation inhibits the *hippo* pathway(*29*), we asked whether YAP localization is altered in HRas-transformed MCF10A cells(*23*). In line with previous findings, we found that HRas-transformation abolished YAP cytoplasmic sequestration at high density (Figure 1e, f, Supplementary Movie 1) (*29*).

A closer inspection of individual cells during monolayer growth revealed large fluctuations in YAP N/C during monolayer growth, with localization inverting within 120 minutes (Figure 2a, Supplementary Movie 2). To characterize these localization fluctuations, we measured YAP N/C ratios over a 24-hour period at a 15-minute sampling frequency. Single cell localization traces revealed rapid changes in YAP N/C ratio, suggesting that YAP localization is dynamically tunable (Figure 2b, c).

As YAP-localization is primarily controlled through phosphorylation (*30*), we hypothesized that modulating upstream kinase activity would alter YAP N/C dynamics. We tested this possibility via HRas transformation which suppresses LATS activity, and Src kinase inhibition which upregulates LATS activity (*29*)(*31*)(*32*). The fluctuation magnitude and frequency were unchanged across conditions (Supplementary Figure 1), but the fraction of cells with at least one fluctuation increased upon PP1 treatment (56% of cells) and decreased upon HRas transformation (6% of cells) compared to untreated MCF10A cells (23% of cells, Figure 2b-d, Supplementary Movie 3). Although N/C fluctuations were largely uncorrelated with neighboring cells (Supplementary Movie 3), there were occasional coordinated fluctuations in cohorts of neighboring cells (Figure 2e-f, Supplementary Movie 4). Our data show that fast localization fluctuations of YAP are common in breast epithelial cells, are regulated by LATS kinases, and can be coordinated among neighboring cells.

Fluctuations in biological systems are often considered crucial for functional and phenotypic “plasticity” (*25*). To delineate the temporal scales over which YAP localization dynamics encode large and rapid changes in environment, we investigated how YAP localization changes upon monolayer wounding. Previous immunofluorescence studies demonstrated fast (~30 minute) nuclear translocation of YAP at the wound edge of mammary epithelial cells (*6*). Surprisingly, real-time tracking of YAP immediately after wounding the monolayer revealed an oscillatory response: rapid nuclear accumulation in edge cells (~1 minute), followed by depletion (lasting ~20 minutes), and finally slow nuclear re-accumulation (~3 hours, Figure 2g, Supplementary Movie 5).

The rapid fluctuations in YAP localization upon wounding hinted at a fast-acting upstream signaling pathway. A fast calcium wave (FCW) within seconds of epithelial wounding has been reported in diverse cell types, including MCF10A (*33*)(*34*)(*35*). We hypothesized that intracellular calcium release may drive the rapid changes in YAP localization. To test this possibility, we released intracellular calcium via thapsigargin (TG) (*36*) treatment, resulting in a bulk YAP translocation cycle similar to that seen at the wound edge: an initial fast depletion (lasting ~25 minutes) followed by slow nuclear enrichment (50 minutes, Figure 2h, Supplementary Movie 6). Ca^{2+} dynamics after TG treatment were tracked using the fast kinetic Ca^{2+} sensor GcAMP6f (*37*), revealing a rapid increase in intracellular Ca^{2+} matching the onset time of nuclear YAP depletion, followed by a slow decay, and then a sustained low amplitude oscillatory phase (Figure 2i). Such collective Ca^{2+} oscillations have been demonstrated at monolayer wound edges (*38*).

Ionomycin, a Ca^{2+} ionophore which also increases intracellular Ca^{2+}, showed similar effects to TG (Supplementary Figure 2a). Simultaneous treatment of ionomycin and the potent phosphatase inhibitor Okadaic acid, which inhibits protein phosphatase 1 upstream of YAP (*39*), led to a similar degree of cytoplasmic sequestration but with minimal recovery, suggesting that Ca^{2+} drives phosphorylation of YAP followed by PP1-dependent dephosphorylation (Supplementary Figure 2a). Previous reports have shown that the release of extracellular ATP may drive FCW at epithelial wound edge (*40*). Although addition of 10mM extracellular ATP induced a similar response as TG and ionomycin, we found there was a sharp dependence on local cellular density, with sparse cells responding minimally (Supplementary Figure 2b). Immunofluorescence imaging in glioblastoma cells by Liu *et al* showed that LATS1/2 is critical to Ca^{2+}-driven phosphorylation and cytoplasmic sequestration of YAP (*41*). Indeed, treatment with the potent protein kinase C inhibitor Go6976 (*41*) delayed depletion and reduced the magnitude of the localization response (Supplementary Figure 2c, Supplementary Movie 6).

We found that the onset of Ca^{2+} release correlated with a rapid decrease in nuclear volume followed by pulses of compression and relaxation corresponding to calcium oscillations (Figure 2j). Since the nuclear membrane mechanically regulates YAP translocation (*42*), we hypothesized that the Ca^{2+}-induced compression of the nucleus may be contributing to the YAP localization reset. To reduce the compressibility of the nucleus, we over-expressed the Δ50LaminA variant which confers increased rigidity to the nucleus (*42*). Indeed, Δ50LaminA overexpression reduced the mean nuclear compression by 48% after TG treatment (Supplementary Figure 3a-b, Supplementary Movie 7) and significantly reduced the Ca^{2+}-induced YAP localization reset, suggesting that the mechanical regulation of the nucleus contributes to YAP localization fluctuations (Supplementary Figure 3c, Supplementary Movie 6).

Next, we asked whether YAP localization resets were somehow connected to the expression of YAP target genes. Indeed, YAP localization changes upon Angiotensin II stimulation have been associated with increased YAP dependent transcription (*43*). We used CRISPR-Cas9 based genome editing to insert a 24X-MS2 transcriptional reporter cassette (*44*) at the 3' UTR of two well-documented YAP responsive genes, Ankyrin Repeat Domain 1 (ANKRD1) (*26*) and Amphiregulin (AREG) (*27*) (Figure 3a). Co-expression of an mNeon-Green fusion of the bacteriophage MS2 coat protein (MCP-mNeon-NLS) (*44*) allowed us to quantify instantaneous transcriptional output by monitoring actively transcribing loci (Figure 3b). This experimental design allowed us to (a) avoid the inherent delays resulting from mRNA export, translation, and FP maturation times seen with synthetic reporters based on fluorescent protein expression driven by YAP-responsive promoter-arrays (*8*) and (b) avoid potential artifacts due to position effects (*45*) that can occur when synthetic reporters are randomly incorporated into the genome.

We used TG treatment to provide a temporally synchronized input to YAP signaling. TG treatment rapidly increased both the number of cells transcribing *ANKRD1* and *AREG* (Figure 3c, d; Supplementary Movie 8) and the intensity of nascent spots (Supplementary Figure 4a). The calcium induced localization reset of YAP and concomitant up-regulation of YAP dependent transcription, point towards a non-linear relationship between YAP localization and target gene transcription contrary to the standard model equating nuclear enrichment with YAP activity. To test the potential connection between localization resets and transcription, we blunted the TG-induced localization resets with Go6976 pre-treatment, which severely attenuated both *AREG* and *ANKRD1* transcriptional responses (Figure 3e-f, Supplementary Figure 4a). To further test a connection between YAP localization resets and native transcriptional responses, we hypothesized that the PP1 Src inhibitor PP1 would also increase YAP responsive transcriptional outputs, based on PP1's ability to increase YAP N/C fluctuations. Indeed, both ANKRD1 and AREG showed moderate increase in transcription following PP1 treatment (Figure 3g-h). PP1 treatment led to an immediate (albeit moderate) increase in ANKRD1 while AREG increased more slowly peaking ~7 hours post treatment (Figure 3g, h). Additionally, PP1 treatment of MCF10A $^{\text{ANKRD1-MS2-KI}}$ cells increased the number of long-lived transcription pulses (Supplementary Figure 4b). Thus, all three interventions (TG, TG/Go6976, and PP1) affected both YAP localization resets and gene expression and did so in a consistent manner.

To test if a fundamental connection exists between YAP shuttling and the transcription of YAP-responsive genes in the context of native cellular processes, we focused on mitotic exit, since mitotic chromatin condensation has been deemed as a major mediator of transcription factor displacement from bulk chromatin(*46*). Recent work has provided evidence for regulation of Hippo signaling by processes intrinsic to cell cycle progression(*47*). We observed that YAP was excluded from condensed chromosomes (Figure 4i) during mitosis, suggesting that localization resets are intrinsic to cell division. Might nuclear re-entry of YAP upon mitotic exit also re-activate YAP-dependent transcription? We approached this question with the real-time transcription reporter lines, by synchronizing cultures to the G1/S phase boundary using a double thymidine block and imaging continuously for 24 hours upon release of the block. Aligning the single cell transcription traces by cytokinesis revealed that both AREG and ANKRD1 transcription peaked over a 2-hour period following mitotic exit (Figure 4j-m; Supplementary Movie 9) before gradually decaying over the next 16 hours (Figure 4l, m). This remarkable pattern suggests that target-gene expression activates shortly after a YAP localization reset and is followed by a currently undiscovered intrinsic inhibitory process despite YAP remaining nuclear. The complex activation and temporal dynamics of YAP-dependent transcription highlights that transcription levels cannot by inferred by a simple nuclear abundance metric for YAP.

Finally, we investigated how localization resets are affected by oncogenic transformation, which permanently alters YAP regulatory circuits (*7*). We found that transformation dampened localization resets (Figure 2c, d) and eliminated cell-density sensing (Figure 1e, f) while increasing transcription output of commonly assayed YAP target genes (Supplementary Figure 5). Further, transformed cell lines (MCF10AT $^{\text{YAP-GFP-KI}}$, SUM159 $^{\text{YAP-GFP-KI}}$, and MDA-MB-231$^{\text{YAP-GFP-KI}}$) showed reduced YAP localization response upon TG treatment (Figure 4a), suggesting that oncogenic transformation perturbs YAP localization control. This is counterintuitive, since, if localization resets drive YAP target gene transcription, why are YAP responsive genes chronically upregulated in transformed cells that lack localization resets?

Perhaps, YAP transcriptional regulation in transformed cells operates through a mode distinct from localization-resets, for example, via modulation of nuclear import and export rates. All three transformed lines had upregulated YAP nuclear export and import rates compared to MCF10A (Figure 4b, 4c). However, MCF10A had the highest *ratio* of import to export ($\bar{k}_{\text{import}}/\bar{k}_{\text{export}}$=3.9) compared to all transformed cell lines (HRas=1.7, SUM159=1.7, MDA-MB-231=1.6). The upregulated import and export rates of YAP in transformed cell lines imply that YAP rapidly equilibrates between the nucleus and cytoplasm. Using an engineered nuclear transport reporter that harbors a nuclear localization signal and a nuclear export signal, we found that the base-line (i.e. non-YAP) nuclear export rates

across all cell lines were not significantly different (Figure 4c), suggesting that YAP transport rates are specifically affected by transformation.

Previous work has shown that YAP has increased interactions with chromatin in cancer-associated fibroblasts (*14*). To understand whether malignant transformation affects YAP-chromatin interactions in breast epithelial cells, we performed high time-resolution FRAP experiments on native YAP-GFP in the nucleus (Figure 4d) and fit data to either pure diffusion or diffusion-reaction models (*48*) (Supplementary Figure 6, Methods). There were striking differences in the degree of YAP-chromatin interactions: ~52% of YAP molecules were effectively bound in MCF10A, whereas in the transformed cell lines, YAP-chromatin interactions were best described by pure diffusion (Supplementary Table 1).

The apparently contrasting observations of higher YAP-chromatin binding and lower YAP activity interactions in untransformed cells may be reconciled by a model where prolonged nuclear retention causes transcriptional inhibition. In this model, the enhanced chromatin interactions may constitute a nonspecific retention mechanism that deactivates YAP. The localization resets oppose this inhibition by transient activation of YAP. On the other hand, Ras-transformation abolishes nuclear retention, allowing escape from compartmentalization-based control through rapid nucleocytoplasmic exchange. Previous work suggests that the increased activity of YAP in Ras-transformed pancreatic cells reflects increased YAP levels (*49*). Our observations of accelerated nucleocytoplasmic exchange and compromised nuclear retention raise the possibility that amplification of YAP-dependent transcription is not merely due to increased expression levels but also to dysregulated nucleocytoplasmic dynamics.

We propose a new regulatory mechanism for YAP dependent transcription in which specific patterns of YAP nuclear exit/reentry are central to gene activation. It has been suggested that nuclear retention can inhibit transcription factor activity through posttranslational modifications which can be reversed through re-localization to the cytoplasmic compartment, as seen in nuclear factor erythroid 2-related factor 2 (Nrf2) (*50*). This raises the intriguing possibility that prolonged nuclear retention deactivates YAP, whereas Ras transformation maintains YAP in a hyper-active form through rapid nucleocytoplasmic turnover (Figure 4f). Modulation of YAP activity in a variety of cellular context is underscored by multiple posttranslational modifications (PTMs). For example, phosphorylation of nuclear YAP at Y357 reduces its transcriptional competence without affecting its localization (*14*). Further exploration of compartment-specific PTMs may offer further insight into the mechanisms behind dynamic transcription control through YAP.

Materials and Methods

Cell culture

MCF10A, MCF10AT were cultured as previously described (*51*). SUM159, MDA-MB-231 were cultured in DMEM + 10% FBS. All cell lines were maintained at 37° C and 5% CO_2 either in tissue culture incubators or microscope incubators.

Drug treatments

Thapsigargin (TG): Alfa Aesar - #J62866. 1mM DMSO stock. Cells were treated at 1 μM and imaged immediately.
Src inhibitor (PP1): Cayman Chemical Company - #14244. 10mM DMSO stock. Cells were treated at 10 μM and imaged after 1 hr for YAP fluctuation experiments or immediately for transcription experiments.
PKC inhibitor (Go 6976): Tocris, #2253. 1mM DMSO stock. Cells were treated at 1 μM for 2 hours before being treated by TG.

Cell line generation and endogenous gene tagging using CRISPR-Cas9

For C terminal tagging of YAP and TEAD with GFP/mCherry we generated donor plasmids for homology dependent repair (HDR) where the general design of the donor plasmid consisted of an upstream homology arm (~1Kb long) followed by GFP/mCherry-(P2A-Puromycin/Hygromycin-stop codon) cassette followed by a downstream homology arm (~1Kb long). MCF10A cells grown to ~80% confluence was trypsinized and electroporated with the donor plasmid, guide RNA plasmid and a plasmid expressing SpCas9 at a ratio of 2:1:1 (total 12ug) using Neon electroporator (Life Technologies) and a 30ms: 1100V: 2pulse electroporation program. Following electroporation cells were grown for three days before initiating antibiotic selection. For antibiotic selection, fresh media containing 1μg/ml Puromycin or 250 μg/ml Hygromycin was added to the cells every two days. Post selection cells were grown in antibiotic free media. For both YAP and TEAD, tagging efficiency was nearly 100% as nearly all cells post-selection showed appropriate localization of the FP tagged proteins and were genomically stable over at least 20 division cycles. For further validation genomic sequences containing the knockins were PCR amplified and sequenced. For generating YAP GFP knockins of MCF10AT, SUM159 and MDA-MB231, cells were electroporated using a Neon electroporator then selected as described above. For MDA-MB231 a 10ms: 1400V: 4pulse electroporation program was used whereas for MCF10AT and SUM159 we used a 30ms: 1100V: 2pulse electroporation program.

For generating cell lines that can report on native transcription kinetics of YAP responsive genes, MCF10A cells were first transfected with a Super Piggy BAC Transposase expression vector (SBI) and a custom generated PiggyBAC vector carrying an MCP-mNeon gene driven by TRE3G promoter and a rTTA3 (tetracycline-controlled transactivator 3)-T2A-Hygromycin cassette driven by a PGK promoter, followed by selection with 250ug/ml hygromycin. To insert a 24X MS2 transcription reporter cassette at the beginning of the 3' UTR of AREG, we generated a donor plasmid for homology dependent knockin where the general design consisted of an upstream homology arm (~1Kb long) followed by a HA tag-P2A-Blasticidine-stop codon-24X MS2 cDNA cassette followed by a downstream homology arm (~1Kb long). For ANKRD1, which had a low CRISPR mediated knockin efficiency, we used a double cut HDR donor plasmid where the "homology-knockin" cassette was flanked by single guide RNA (sgRNA)-PAM sequence on either side. This greatly increased knockin efficiency for ANKRD1. Cells were selected with 10 μg/ml Blastcidine.
For calcium sensing, cells were transduced with lentiviral particles reconstituted from a lentiviral vector expressing GcAMP6f from a constitutively active CMV promoter.

To minimize any potential confounding effect of differences in source of origin of MCF10A and MCF10AT, we generated a constitutively active H-Ras (H-RasG12V) transformed MCF10AYAP-GFP-KI cell line using lentiviral transduction and subsequent selection for neomycin resistance using Geneticin (400 μg/mL). This cell line was used specifically for the line-FRAP, and import/export measurements.

Details of Cell lines

Cell line	Source cell line	Method of cell line generation	Antibiotic resistance

MCF 10A YAP-eGFP	MCF10A	CRISPR knock in	Puromycin
MCF 10AT YAP-eGFP	MCF10AT	CRISPR knock in	Puromycin
MCF 10AT YAP-eGFP	MCF10A YAP-eGFP	CRISPR knock in + HRas Lentiviral transduction	Neomycin
SUM159 YAP-eGFP	SUM159	CRISPR knock in	Puromycin
MDA MB 231 YAP-eGFP	MDA MB 231	CRISPR knock in	Puromycin
MCF 10A YAP-eGFP + TEAD1 mCherry	MCF10A	Dual CRISPR knock in	Puromycin + Hygromycin
MCF 10A MCP mNeon	MCF10A	PiggyBAC transposition	Hygromycin
MCF 10A MCP mNeon Areg 24X MS2	MCF10A MCP mNeon	CRISPR knock in	Hygromycin + Blasticidin
MCF 10A MCP mNeon ANKRD1 24X MS2	MCF10A MCP mNeon	CRISPR knock in	Hygromycin + Blasticidin
MCF 10A GcAMP6f	MCF 10A	Lenti Viral transduction	Puromycin
MCF10A YAP-eGFP + LAM del50 mCherry	MCF 10A YAP-eGFP	PiggyBAC transposition	Hygromycin
MCF 10A NLS-GFP_{2X}-NES	MCF 10A	Lenti Viral transduction	Neomycin
MCF 10AT NLS-GFP_{2X}-NES	MCF 10AT	Lenti Viral transduction	Neomycin
SUM 159 NLS-GFP_{2X}-NES	SUM 159	Lenti Viral transduction	Neomycin
MDA MB231 NLS-GFP_{2X}-NES	MDA MB231	Lenti Viral transduction	Neomycin

Guide sequences used for CRISPR knockin

YAP	TTAGAATTCAGTCTGCCTGA
TEAD	GGCTTGTAAAGGACTGAACA
AREG	AAGAAACTTCGACAAGAGAA
ANKRD1	TCTCGCATAGCTACATTCTG

Microscopy

Live imaging was done on either Zeiss LSM700 or an Olympus FV10i. Cells plated on fibronectin-coated MATTEK dishes (35mm, No. 1.5 glass) were imaged either with 63x/1.40 oil immersion (Zeiss) or 60x/1.2 water immersion (Olympus) objective. All multi-day image acquisitions were carried out on Olympus FV10i.

All photo-bleaching experiments were performed on Zeiss LSM700 using the following parameters:

Photobleaching experiments	Laser (nm)	Frame rate	# pre-scan frames	# bleach scans	# post-scan frames
Import/export	488	10 s	1	12	12
YAP spatiotemporal FRAP	488	4.6 ms	500	8	1000

Image analysis

All calculations and analysis were performed using MATLAB, Python, and ImageJ. The cell/spot segmentation, tracking, and analysis functions are publicly available here: https://github.com/jmfrank/track_analyzer. FRAP model fitting was implemented in Mathematica based on Stasevich et al (*48*).

Cell tracking

Cell tracking was performed following these steps: (1) anisotropic diffusion filtering and sum of signal derivatives, (2) applying global threshold to identify nuclei, (3) seeded watershed segmentation to breakup regions into single nuclei, (4) frame-to-frame tracking using a distance minimizing linking algorithm. Tracking was verified by eye using a GUI, and artifactual tracks were flagged and excluded by downstream analysis.

N/C ratio

In this work, the N/C ratio is defined as the ratio of nuclear to cytoplasmic concentrations of YAP (or TEAD), assessed by the mean fluorescence intensity in the nucleus and cytoplasmic volumes after subtracting fluorescence background. The masks used to measure N/C was a 3-plane volume, centered by the plane with maximum Sir-DNA intensity. Because YAP is physically excluded from the nucleoli, we removed the nucleolar regions (determined by the lower 35^{th} percentile of intensities within the nucleus boundary). The cytoplasmic region was determined by generating a mask extending 0.5 um from the nucleus boundary into the cytoplasm. Because TEAD is mostly nuclear, we used the TEAD signal to segment the nucleus rather than Sir-DNA.

Local cell density

To account for variable density in a growing monolayer, we estimated the local cell density for each detected cell as the number of cell centroids found within a search radius of 250 pixels (69 μm) of the cell of interest centroid.

YAP N/C fluctuation analysis

Rapid changes in YAP signal were defined as signals that are continuously increasing or decreasing by at least 0.12 (N/C magnitude). If the signal did not change at least 0.005 over a 3-frame window, then the signal was considered stagnated and continuity was broken.

Wound assay

MCF10A cells were seeded on MATTEK imaging dishes at 50% confluency. After 3 days of growth, the very dense monolayer was imaged (Figure 2g pre-wound). The dish was then gently scratched with a 20uL pipette tip and immediately imaged. About a 1-minute delay between wounding and the first image due to incubator adjustment and microscope focusing.

GcAMP6f imaging

Similar to the YAP signal, we measured the GcAMP6f signal as the average of a 0.5 um wide contour extending into the cytoplasm from the nuclear boundary, as the GcAMP6f signal is mostly excluded from the nucleus.

Nascent transcription

Nucleus segmentation was performed in 3D to ensure each nascent transcription spot was located within the nucleus. Although we sorted MCP-mNeon expressing cells, the expression per cell was variable, requiring local thresholding to segment cells with different expression levels. This was done using the following steps:
[1] Applying filtering (as described in the 2D Sir-DNA segmentation)
[2] Finding local maxima
[3] Applying a lower-bound threshold to include all regions containing a local maxima
[4] Looping over all regions found in step 3, use the derivative of the intensity-percentile distribution (dI/dP) of pixel intensities to determine the local threshold. A peak in dI/dP indicates the background to foreground boundary (see plot below). With no significant peak, the region is properly segmented. Because the local threshold is not the same for all regions, one needs to look at the histogram information in terms of percentile to find the foreground vs background for each sub-region.

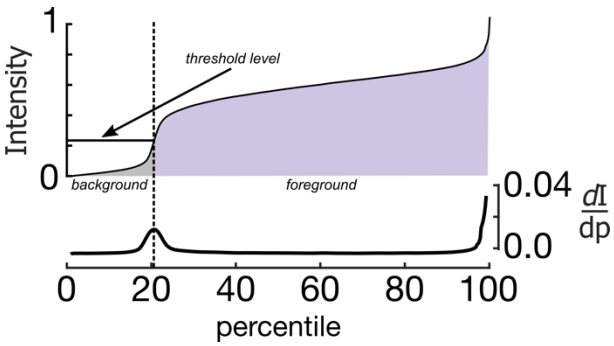

[5] Applying a seeded watershed to separate connecting nuclei.

After identifying cell nuclei, actively transcribing cells were identified by looking for a sharp, bright signal (for MCP-mNeon) within the segmented nuclei. Spots were detected in two steps to ensure robust quantification:

[1] Potential spots were first identified by using a Laplacian of Gaussian filter, followed by a local thresholding by identifying potential spots as regions of pixel intensity greater than 99.97th percentile of all pixels within a particular nucleus.
[2] An integrated intensity threshold is then applied to these potential spots from step 1. For each potential spot, a background measurement was made using a shell mask centered at the centroid of the potential spot (inner diameter 7px, outer diameter 9 pixels). The integrated intensity is the sum of all pixel values within the inner shell region (i.e. pixels located less than 3.5 pixels from centroid).
[3] Particle tracking was applied to nascent spots to gather statistics on pulse duration and intensity.

Analysis of mitotic cells

Mitotic cells were manually annotated using a GUI to mark the time of cytokinesis, parent cell, and daughter cells for each division. The data extracted from the cells is then aligned by the time of cytokinesis. To create the YAP N/C trace through division, the N/C trace of the parent cell was concatenated with the mean N/C values of the daughter cells. Nascent transcription through mitosis was evaluated by measuring the fraction of cells with at least one nascent transcription spot and normalizing the pre-mitosis fraction to 1. Because the pre-mitosis nucleus is diploid, there are 2X copies of the MS2 gene cassette and each daughter receives 1X copies. Therefore, the post-mitosis fraction of cells is measured by whether *either* of the daughters are transcribing, which means the same number of MS2 gene cassettes are monitored before and after division.

Spatiotemporal line FRAP of nuclear YAP-eGFP

We found that the YAP-eGFP recovery is extremely rapid, so we opted to use a circular ROI for bleaching (10 pixel radius, 0.9 μm) but a line ROI (2 pixel wide) bisecting the bleach spot to monitor the recovery, allowing a 4.6 millisecond frame time using the Zeiss 700. For each bleach acquisition, a background measurement was taken at the same position after waiting 15 seconds after the bleach acquisition completed. The final spatiotemporal recovery curve was generated by: (1) Normalizing fluorescence and correcting for acquisition bleaching, (2) averaging across the 2-pixel wide line, and (3) finding the bleach-center by Gaussian fitting and then averaging from multiple experiments. First, we fit the mean recovery curve for each condition to both a pure diffusion and reaction-diffusion model (Supplementary Figure 6). In order to estimate the experimental error for the parameters, we fit 30 bootstrapped samplings (5 experiments per bootstrap) as individual experiments were too noisy to provide accurate fits to the models. The data in Supplementary Table 1 is the mean and standard deviation of each parameter from the 30 bootstraps samples.

For MCF10A, the reaction-diffusion model fit had decreased sum of squared residuals (SSD), while the pure diffusion model provided an unrealistically low diffusion rate, suggesting that significant binding accounts the relatively slow FRAP recovery. For MCF10A+HRas, SUM159, and MDA-MB-231, the reaction-diffusion model slightly decreased SSD compared to pure-diffusion, however the effective diffusion was very large, ranging between 38 and 45 μm^2/s, while the pure diffusion model diffusion coefficient ranged between 24 and 26 μm^2/s. Previously reported

work suggests that the diffusion coefficient for a 100 kDa protein is approximately 21 $\mu m^2/s$ (*52*). Therefore, nuclear YAP kinetics in MCF10A+HRas, SUM159, and MDA-MB-231 are best described by pure-diffusion, and binding is negligible at the experimental resolution we could achieve.

Import / export rates of YAP and synthetic NLS-NES construct

The first-order nuclear import and export rate of either YAP or the NLS-NES construct (NLS-GFP_{2X}-NES) was measured by monitoring the nuclear intensity after bleaching either the nucleus or cytoplasm. First, a bright field image was used to draw a spline ROI defining the contour of the nucleus or cytoplasm. After bleaching ROI, time-lapse confocal imaging was used to monitor the recovery. We found that full recovery of YAP after nuclear/cytoplasm bleaching was on the time-scale of ~1-2 minutes. As nuclear volume is essentially constant on this time scale, and YAP signal is homogenous and rapidly diffuses, we measured the average fluorescence intensity of an ROI within the nucleus over time. We then monitored the change of this signal from the first post-bleach time point. The first-order import or export rate is then approximated by the slope of a linear fit to the change in signal over the first 30 seconds (frames 1-4) after bleaching. By dividing the signal trace by the post-bleach intensity of the nucleus (export) or cytoplasm (import), we measure the *specific* first-order transport rate which is independent of protein expression in the cell.

RNA-seq relative gene expression

Raw reads of RNA-seq for MCF10A and MCF10AT were downloaded from GEO-Depositions (MCF10A-HRas: GSE81593(*53*); MCF10A: GSE75168 (*54*)). The reads were first trimmed with cutadapt to remove adapters and low-quality reads. The reads then were aligning to human genome hg19 using HISAT2 with default parameters. Gene expression counts were obtained from bam files using htseq-count. The relative expression between MCF10AT and MCF10A was computed per gene as the ratio of counts in MCF10AT divided by counts in MCF10A. This ratio was corrected using the average ratio of 25 house-keeping genes(*55*)(*56*)(*57*) between MCF10AT and MCF10A.

Acknowledgments

This work was partially supported by the National Institutes of Health (NIH) National Institute Of General Medical Sciences (NIGMS)/National Cancer Institute (NCI) Grant GM77856, NCI Physical Sciences Oncology Center Grant U54CA143836, National Science Foundation Graduate Fellowship Program #DGE-114747, and National Institute Of Biomedical Imaging And Bioengineering (NIBIB)/4D Nucleome Roadmap Initiative 1U01EB021237. We thank Lacramioara Bintu (Assistant Professor, Bioengineering, Stanford), Timothy J. Stasevich (Assistant Professor, Biochemistry & Molecular Biology, Colorado State University) and Pere Roca-Cusachs (Institute of Bioengineering of Catalonia) for their comments on the manuscript.

Author Contributions

R.P.G and J.M.F and J.T.L conceived the project. J.M.F and R.P.G designed research. R.P.G generated the CRISPR/Cas9 genomic knockins. J.M.F, R.P.G and Q.S did experiments. J.M.F analyzed data and generated movies. R.P.G, J.M.F and J.T.L wrote the paper.

References

1. S. Piccolo, S. Dupont, M. Cordenonsi, The Biology of YAP/TAZ: Hippo Signaling and Beyond. *Physiol. Rev.* (2014), doi:10.1152/physrev.00005.2014.
2. F. X. Yu, B. Zhao, K. L. Guan, Hippo Pathway in Organ Size Control, Tissue Homeostasis, and Cancer. *Cell* (2015), , doi:10.1016/j.cell.2015.10.044.
3. T. Moroishi, C. G. Hansen, K. L. Guan, The emerging roles of YAP and TAZ in cancer. *Nat. Rev. Cancer* (2015), doi:10.1038/nrc3876.
4. S. M, Yes-associated protein (YAP65) is a proline-rich phosphoprotein that binds to the SH3 domain of the Yes proto-oncogene product.le. *Oncogene* (1994).
5. F. Kanai *et al.*, TAZ: A novel transcriptional co-activator regulated by interactions with 14-3-3 and PDZ domain proteins. *EMBO J.* (2000), doi:10.1093/emboj/19.24.6778.
6. M. Aragona *et al.*, A mechanical checkpoint controls multicellular growth through YAP/TAZ regulation by actin-processing factors. *Cell* (2013), doi:10.1016/j.cell.2013.07.042.
7. F. Zanconato, M. Cordenonsi, S. Piccolo, YAP/TAZ at the Roots of Cancer. *Cancer Cell* (2016), , doi:10.1016/j.ccell.2016.05.005.
8. S. Dupont *et al.*, Role of YAP/TAZ in mechanotransduction. *Nature* (2011), doi:10.1038/nature10137.
9. B. Zhao *et al.*, Inactivation of YAP oncoprotein by the Hippo pathway is involved in cell contact inhibition and tissue growth control. *Genes Dev.* (2007), doi:10.1101/gad.1602907.
10. J. E. Purvis, G. Lahav, Encoding and decoding cellular information through signaling dynamics. *Cell* (2013), , doi:10.1016/j.cell.2013.02.005.
11. E. Batchelor, A. Loewer, C. Mock, G. Lahav, Stimulus-dependent dynamics of p53 in single cells. *Mol. Syst. Biol.* (2011), doi:10.1038/msb.2011.20.
12. L. Ashall *et al.*, Pulsatile stimulation determines timing and specificity of NF-κB-dependent transcription. *Science (80-.).* (2009), doi:10.1126/science.1164860.
13. A. Elosegui-Artola *et al.*, Force Triggers YAP Nuclear Entry by Regulating Transport across Nuclear Pores. *Cell* (2017), doi:10.1016/j.cell.2017.10.008.
14. N. Ege *et al.*, Quantitative Analysis Reveals that Actin and Src-Family Kinases Regulate Nuclear YAP1 and Its Export. *Cell Syst.* (2018), doi:10.1016/j.cels.2018.05.006.
15. S. A. Manning *et al.*, Dynamic Fluctuations in Subcellular Localization of the Hippo Pathway Effector Yorkie In Vivo. *Curr. Biol.* (2018), doi:10.1016/j.cub.2018.04.018.
16. K. C. Lin *et al.*, Regulation of Hippo pathway transcription factor TEAD by p38 MAPK-induced cytoplasmic translocation (Nature Cell Biology, (2017), 19, 8, (996-1002), 10.1038/ncb3581). *Nat. Cell Biol.* **20**, 1098 (2018).
17. L. B. Andrews, A. A. K. Nielsen, C. A. Voigt, Cellular checkpoint control using programmable sequential logic. *Science (80-.).* (2018), doi:10.1126/science.aap8987.
18. N. Rosenfeld, J. W. Young, U. Alon, P. S. Swain, M. B. Elowitz, Gene regulation at the single-cell level. *Science (80-.).* (2005), doi:10.1126/science.1106914.
19. B. P. Kramer, M. Fussenegger, Hysteresis in a synthetic mammalian gene network. *Proc. Natl. Acad. Sci.* (2005), doi:10.1073/pnas.0500345102.
20. O. Purcell, T. K. Lu, Synthetic analog and digital circuits for cellular computation and memory. *Curr. Opin. Biotechnol.* (2014), , doi:10.1016/j.copbio.2014.04.009.
21. N. Balaskas *et al.*, Gene regulatory logic for reading the sonic hedgehog signaling gradient in the vertebrate neural tube. *Cell* (2012), doi:10.1016/j.cell.2011.10.047.
22. P. Mali *et al.*, RNA-guided human genome engineering via Cas9. *Science (80-.).* (2013), doi:10.1126/science.1232033.
23. J. Russo, L. Tait, I. H. Russo, Morphological expression of cell transformation induced by c-Ha-ras oncogene in human breast epithelial cells. *J Cell Sci* (1991).
24. D. M. Suter *et al.*, Mammalian genes are transcribed with widely different bursting kinetics. *Science (80-.).* (2011), doi:10.1126/science.1198817.
25. K. Sato, Y. Ito, T. Yomo, K. Kaneko, On the relation between fluctuation and response in biological systems. *Proc. Natl. Acad. Sci.* (2003), doi:10.1073/pnas.2334996100.
26. K.-C. Wang *et al.*, Flow-dependent YAP/TAZ activities regulate endothelial phenotypes and atherosclerosis. *Proc. Natl. Acad. Sci.* (2016), doi:10.1073/pnas.1613121113.
27. J. Zhang *et al.*, YAP-dependent induction of amphiregulin identifies a non-cell-autonomous

component of the Hippo pathway. *Nat. Cell Biol.* (2009), doi:10.1038/ncb1993.
28. B. Zhao *et al.*, TEAD mediates YAP-dependent gene induction and growth control. *Genes Dev.* (2008), doi:10.1101/gad.1664408.
29. S. J. Rawat *et al.*, H-ras Inhibits the Hippo Pathway by Promoting Mst1/Mst2 Heterodimerization. *Curr. Biol.* (2016), doi:10.1016/j.cub.2016.04.027.
30. Z. Meng, T. Moroishi, K. L. Guan, Mechanisms of Hippo pathway regulation. *Genes Dev.* (2016), , doi:10.1101/gad.274027.115.
31. N. G. Kim, B. M. Gumbiner, Adhesion to fibronectin regulates Hippo signaling via the FAK-Src-PI3K pathway. *J. Cell Biol.* (2015), doi:10.1083/jcb.201501025.
32. Y. Si *et al.*, Src Inhibits the hippo tumor suppressor pathway through tyrosine phosphorylation of Lats1. *Cancer Res.* (2017), doi:10.1158/0008-5472.CAN-17-0391.
33. P. J. Sammak, L. E. Hinman, P. O. Tran, M. D. Sjaastad, T. E. Machen, How do injured cells communicate with the surviving cell monolayer? *J. Cell Sci.* (1997).
34. V. E. Klepeis, A. Cornell-Bell, V. Trinkaus-Randall, Growth factors but not gap junctions play a role in injury-induced Ca2+ waves in epithelial cells. *J Cell Sci* (2001), doi:10.1016/j.jana.2012.06.007.
35. C. Justet, J. A. Hernández, A. Torriglia, S. Chifflet, Fast calcium wave inhibits excessive apoptosis during epithelial wound healing. *Cell Tissue Res.* (2016), doi:10.1007/s00441-016-2388-8.
36. J. Lytton, M. Westlin, M. R. Hanley, Thapsigargin inhibits the sarcoplasmic or endoplasmic reticulum Ca-ATPase family of calcium pumps. *J. Biol. Chem.* (1991), doi:VL - 266.
37. T. W. Chen *et al.*, Ultrasensitive fluorescent proteins for imaging neuronal activity. *Nature* (2013), doi:10.1038/nature12354.
38. J. Lembong, B. Sabass, H. A. Stone, Calcium oscillations in wounded fibroblast monolayers are spatially regulated through substrate mechanics. *Phys. Biol.* (2017), doi:10.1088/1478-3975/aa6b67.
39. P. Wang *et al.*, PP1A-mediated dephosphorylation positively regulates YAP2 activity. *PLoS One* (2011), doi:10.1371/journal.pone.0024288.
40. L. N. Handly, R. Wollman, Wound-induced Ca 2+ wave propagates through a simple release and diffusion mechanism . *Mol. Biol. Cell* (2017), doi:10.1091/mbc.e16-10-0695.
41. Z. Liu *et al.*, Induction of store-operated calcium entry (SOCE) suppresses glioblastoma growth by inhibiting the Hippo pathway transcriptional coactivators YAP/TAZ. *Oncogene* (2018), , doi:10.1038/s41388-018-0425-7.
42. J. Swift *et al.*, Nuclear lamin-A scales with tissue stiffness and enhances matrix-directed differentiation. *Science (80-.).* (2013), doi:10.1126/science.1240104.
43. J. Wang, J. Sinnett-Smith, J. V. Stevens, S. H. Young, E. Rozengurt, Biphasic regulation of Yes-associated Protein (YAP) cellular localization, phosphorylation, and activity by G proteincoupled receptor agonists in intestinal epithelial cells: A novel role for Protein Kinase D (PKD). *J. Biol. Chem.* **291**, 17988–18005 (2016).
44. E. Bertrand *et al.*, Localization of ASH1 mRNA particles in living yeast. *Mol. Cell* (1998), doi:10.1016/S1097-2765(00)80143-4.
45. W. Akhtar *et al.*, Chromatin position effects assayed by thousands of reporters integrated in parallel. *Cell* (2013), doi:10.1016/j.cell.2013.07.018.
46. M. A. Martínez-Balbás, A. Dey, S. K. Rabindran, K. Ozato, C. Wu, Displacement of sequence-specific transcription factors from mitotic chromatin. *Cell* (1995), doi:10.1016/0092-8674(95)90231-7.
47. W. Kim *et al.*, Hippo signaling is intrinsically regulated during cell cycle progression by APC/CCdh1. *Proc. Natl. Acad. Sci. U. S. A.* (2019), doi:10.1073/pnas.1821370116.
48. T. J. Stasevich, F. Mueller, D. T. Brown, J. G. McNally, Dissecting the binding mechanism of the linker histone in live cells: An integrated FRAP analysis. *EMBO J.* (2010), doi:10.1038/emboj.2010.24.
49. W. Zhang *et al.*, Downstream of mutant KRAS, the transcription regulator YAP is essential for neoplastic progression to pancreatic ductal adenocarcinoma. *Sci. Signal.* (2014), doi:10.1126/scisignal.2005049.
50. M. Xue *et al.*, Frequency modulated translocational oscillations of Nrf2, a transcription factor functioning like a wireless sensor. *Biochem. Soc. Trans.* (2015), doi:10.1042/BST20150060.
51. J. Debnath, S. K. Muthuswamy, J. S. Brugge, Morphogenesis and oncogenesis of MCF-10A mammary epithelial acini grown in three-dimensional basement membrane cultures. *Methods*

(2003), , doi:10.1016/S1046-2023(03)00032-X.

52. N. Dross *et al.*, Mapping eGFP oligomer mobility in living cell nuclei. *PLoS One* (2009), doi:10.1371/journal.pone.0005041.
53. K. E. Yoh *et al.*, Repression of p63 and induction of EMT by mutant Ras in mammary epithelial cells. *Proc. Natl. Acad. Sci.* (2016), doi:10.1073/pnas.1613417113.
54. T. L. Messier *et al.*, Histone H3 lysine 4 acetylation and methylation dynamics define breast cancer subtypes. *Oncotarget* (2016), doi:10.18632/oncotarget.6922.
55. E. Eisenberg, E. Y. Levanon, Human housekeeping genes, revisited. *Trends Genet.* (2013), , doi:10.1016/j.tig.2013.05.010.
56. A. Curina *et al.*, High constitutive activity of a broad panel of housekeeping and tissue-specific cis-regulatory elements depends on a subset of ETS proteins. *Genes Dev.* (2017), doi:10.1101/gad.293134.116.
57. S. Moein, S. Javanmard, M. Abedi, M. Izadpanahi, Y. Gheisari, Identification of Appropriate Housekeeping Genes for Gene Expression Analysis in Long-term Hypoxia-treated Kidney Cells. *Adv. Biomed. Res.* (2017), doi:10.4103/2277-9175.200790.

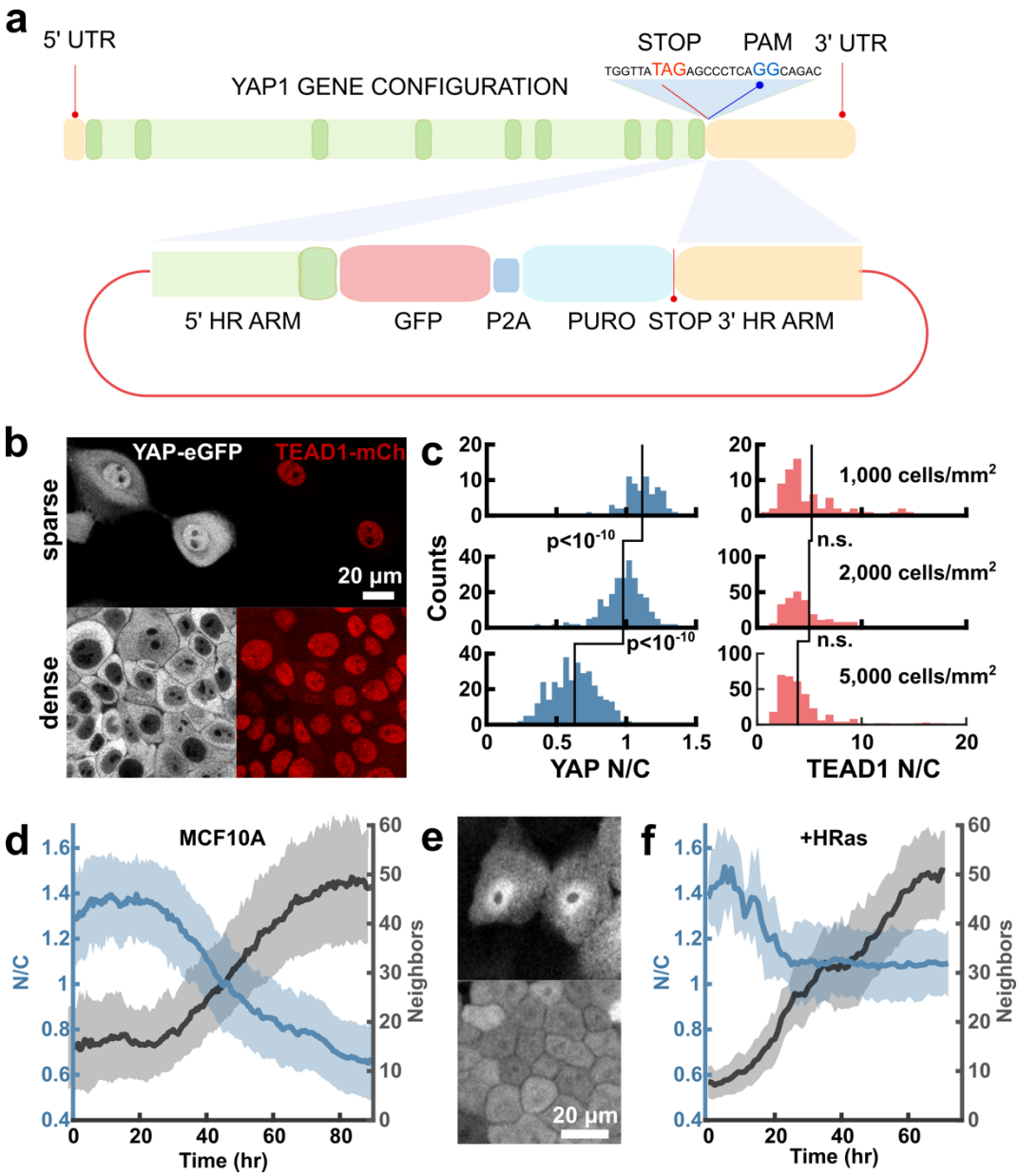

Figure 1: **Characterization of YAP and TEAD genome-knockin cell lines**. (**a**) Cartoon of CRISPR-Cas9 based insertion of eGFP-P2A-puromycin cassette at 3' end of the YAP gene. (**b**) Dense and sparse MCF10A cells with YAP-eGFP and TEAD1-mCherry dual CRISPR knockin. (**c**) N/C of YAP and TEAD1 in MCF10A as a function of density. (**d**) Time-lapse of YAP-eGFP nuclear/cytoplasmic ratio (N/C) during monolayer growth for MCF10A (solid line is mean value, and shading is standard deviation) (N=915 cell tracks). (**e**) Native YAP-eGFP expression/localization in sparse and dense cultures of MCF10A-HRas (MCF10AT). (**f**) Time-lapse of YAP-eGFP nuclear/cytoplasmic ratio (N/C) during monolayer growth for MCF10AT (N=1478 cell tracks).

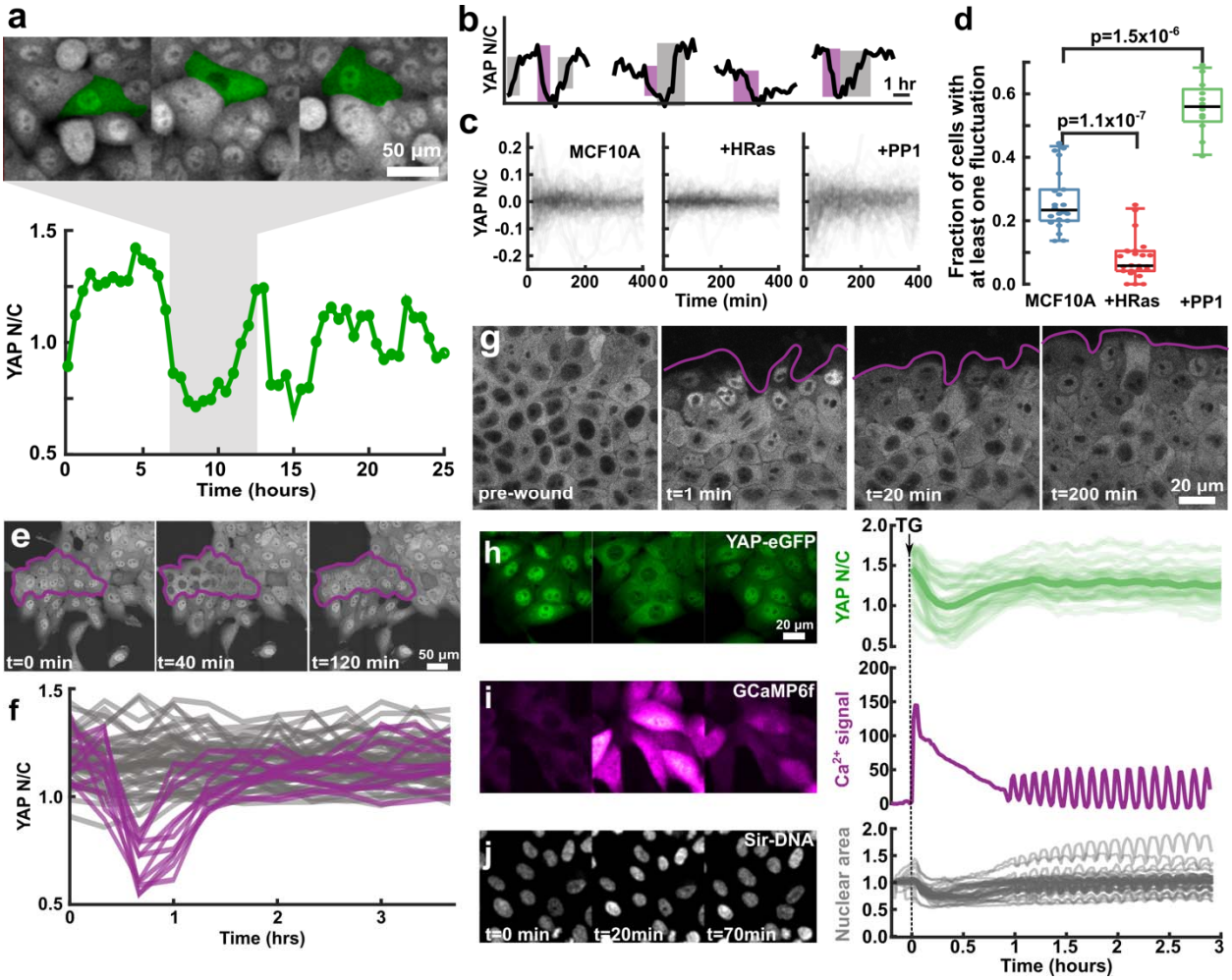

Figure 2: Baseline (minute-scale) fluctuations in YAP localization. (**a**) N/C trace of an individual MCF10A cell in monolayer and corresponding fluorescence image (cell of interest is false-colored in green). (**b**) Example traces of YAP N/C over time with large changes in signal highlighted by grey (increase) and purple (decrease) in MCF10A cells. (**c**) Overlay of YAP N/C traces for MCF10A, MCF10A+HRas, and MCF10A+PP1. Each plot contains 200 traces randomly selected from the pool of all tracks collected from each condition. The mean value is subtracted from each trace to allow visual comparison. (**d**) Mean fraction of cells per ROI (0.0171 mm^2) with at least one detectable fluctuation (24 ROIs for each condition compiled from two independent experiments). (**e**) Fluorescence images of coordinated localization reset. Magenta line encloses the cohort of cells that show reset. (**f**) YAP N/C traces for cells showing coordinated fluctuation (purple) and cells showing invariant YAP N/C (gray). (**g**) Time course of YAP-eGFP localization in MCF10A cells at a wound edge. Wound edge highlighted in magenta. (**b**) YAP localization, (**c**) cytoplasmic calcium signal, and (**d**) nuclear shape at different time points after induction of SOCE using 1uM thapsigargin. YAP N/C traces are from 43 cells and 2 independent experiments. Nuclear area trace and GCaMP6f Ca^{2+} trace are from 42 cells and 2 independent experiments.

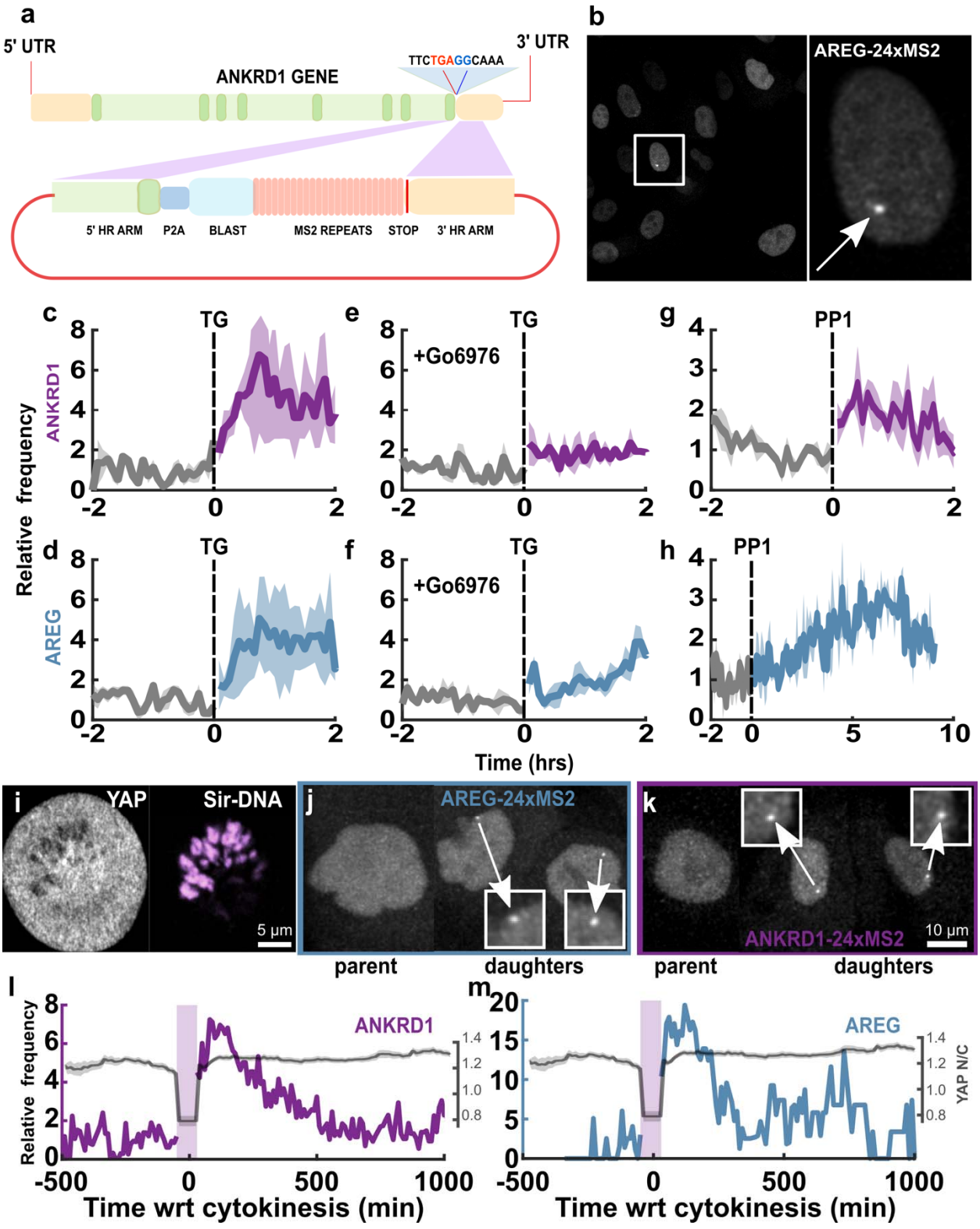

Figure 3: Transcription dynamics of YAP target genes. (**a**) Cartoon showing strategy for knocking in an MS2 transcription reporter cassette at the end of the coding sequence of ANKRD1 gene. (**b**) Representative image of

MCF10A$^{AREG\text{-}MS2\text{-}KI}$ cells co-expressing MCP-mNeon. Inset: A typical nascent transcription spot. (**c-h**) Mean transcriptional frequency before and after drug treatment. Transcriptional frequency was normalized to 1 for the 2-hr pre-treatment period. (**c**, **d**) Treatment with TG, mean+/-STD of three experiments for ANKRD1 (c) and AREG (d). (**e**, **f**) Pre-treatment with 1μM Go6976, followed by TG, mean+/-STD of three experiments for ANKRD1 (e) and AREG (f). (**g**, **h**) Treatment with 1uM PP1, mean+/-STD of 2 (ANKRD1) (g) and 3 (AREG) (h) experiments. (**i**) YAP localization (grey) in a dividing cell (condensed chromatin shown in magenta). (**j, k**) Example of MCF10A$^{AREG\text{-}MS2\text{-}KI}$ (j) and MCF10A$^{ANKRD1\text{-}MS2\text{-}KI}$ (k) cells going through mitosis. Insets show nascent transcription spots in both daughter cells. (**l, m**) *Left axis:* Mean transcription frequency of cells showing transcription reset after mitosis for ANKRD1 (l) and AREG (m). Mitotic events collected from two independent experiments for both ANKRD1 (N=39 divisions) and AREG (N=25 divisions). *Right axis:* mean YAP N/C during division (N=24 divisions). The N/C ratio during mitosis was calculated as the mean value from 7 high-magnification images of mitotic cells expressing YAP (as shown in i).

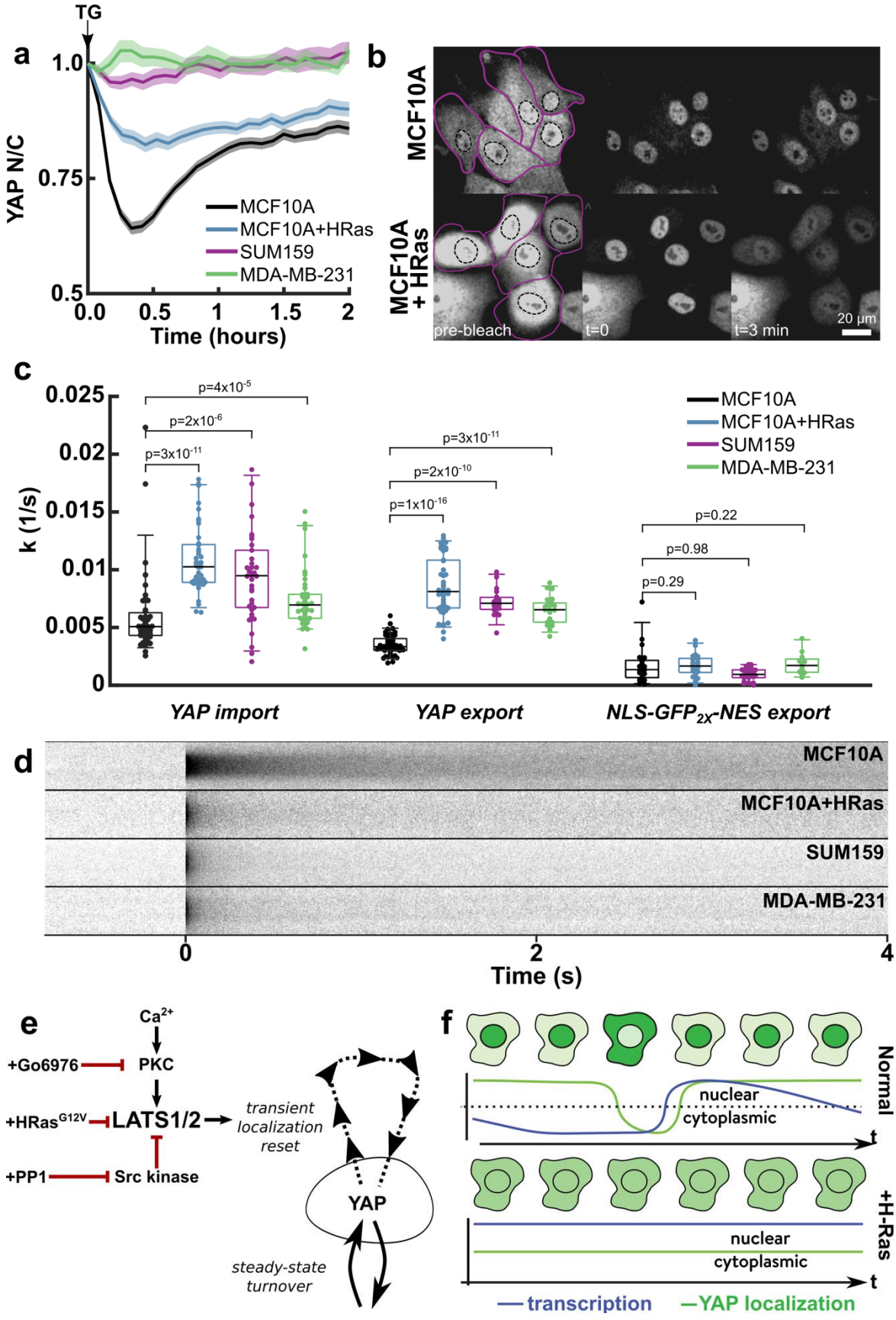

Figure 4: Ras transformation alters YAP dynamics. (**a**) Mean YAP N/C after TG treatment for MCF10A (N=157 tracks), MCF10A + HRas (N=75 tracks), SUM159 (N=70 tracks), MDA-MB-231 (N=101 tracks). (**b**) Representative images of FRAP experiments where cytoplasmic pool of YAP-eGFP is bleached and the nuclear pool is tracked over time. Nuclear boundaries are drawn with dashed black line while cytoplasm boundaries are drawn with solid purple line. HRas transformed cells show significant re-distribution by 3 minutes compared to MCF10A control. (**c**) Distribution of specific import and export rates of YAP, and the export rate of NLS-eGFP2x-NES for MCF10A (N YAP-imp=43, N YAP-exp=49, N exp=21), MCF10A + HRas (N YAP-imp=41, N YAP-exp=46, N exp=21), SUM159 (N YAP-imp=38, N YAP-exp=19, N exp=27), and MDA-MB-231 (N YAP-imp=38, N YAP-exp=23, Nexp=12) YAP-GFP knockin cell lines. P-values are calculated from one-sided Mann-Whitley U-test. Box and whisker lines: black-center line is median value, box-bounds are inter-quartile range, and whiskers are 0.05 and 0.95 quantiles. (**d**) Carpet plot generated from the average line FRAP of YAP-eGFP in various cell lines. (**e**) Summary of induction and modulation of transient YAP localization resets through LATS kinase. (**f**) Proposed model for the relationship between YAP dynamics and YAP responsive transcription. Dashed line represents N/C=1.

Supplementary Figures

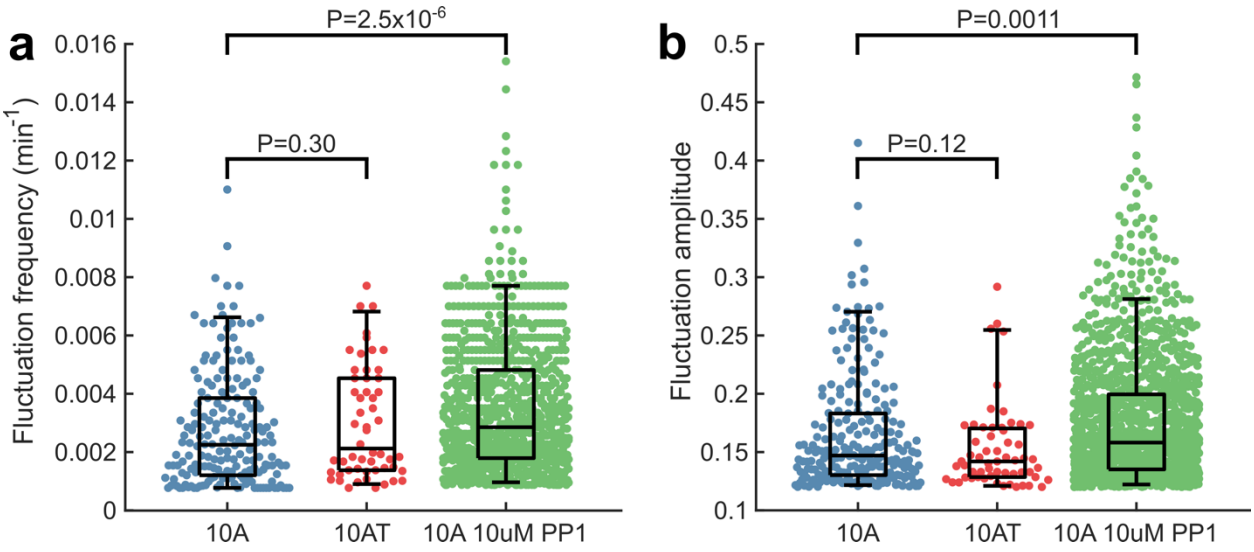

Supplementary Figure 1. YAP N/C pulse density and amplitude analysis under different conditions (10A, 10A+HRas, 10A+PP1). P-values are from two-sided Mann-Whitney U-test.

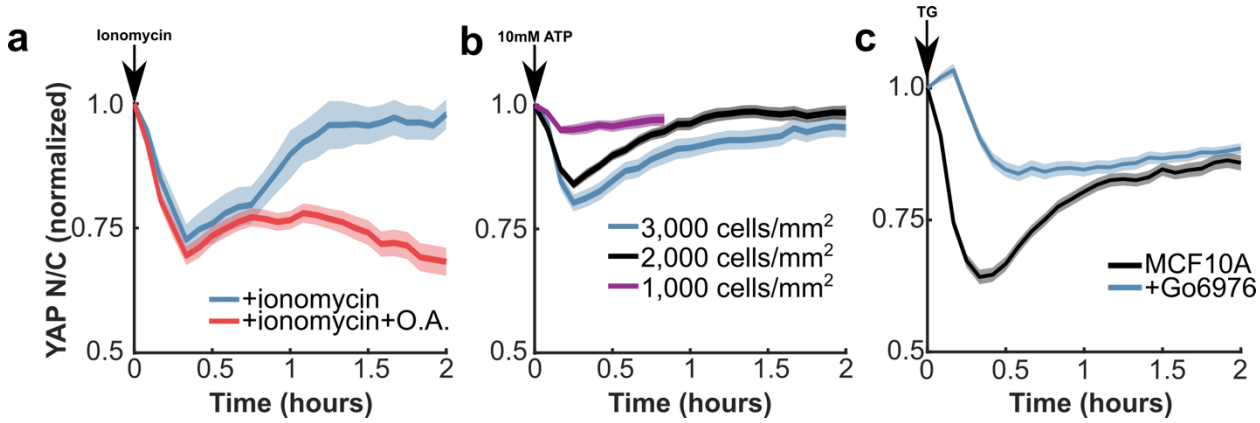

Supplementary Figure 2: Mechanism of YAP spatial reset. (**a-c**) Mean YAP N/C for cells tracked over time under various conditions (All data are normalized to initial time point). (**a**) Treatment with ionomycin (N=47 tracks) or ionomycin and Okadaic acid (N=104 tracks). (**b**) Treatment with 10mM ATP at cell densities of 1,000 cells/mm^2 (N=80 tracks), 2,000 cells/mm^2 (N=162 tracks), and 3,000 cells/mm^2 (N=186 tracks). (**c**) Go6976 pre-treatment + TG (N=104 tracks).

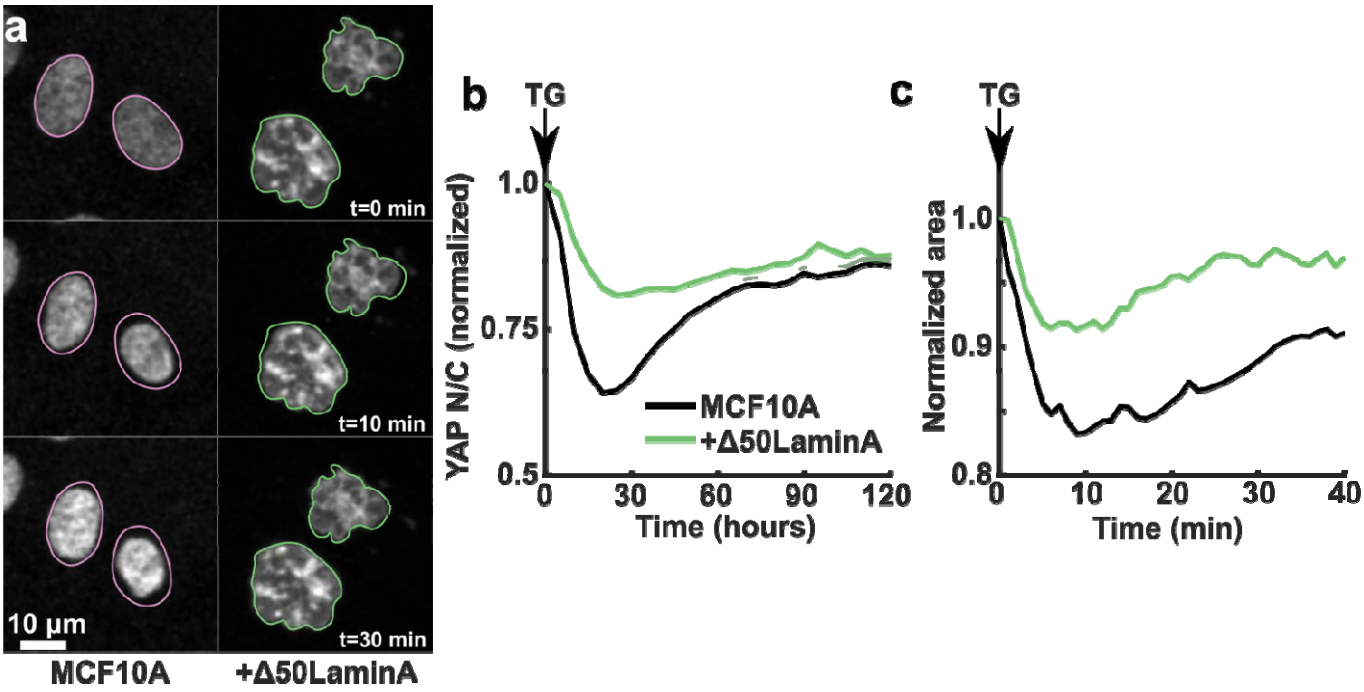

Supplementary Figure 3: Nuclear membrane integrity regulates YAP localization reset. (**a**) Representative images of the nuclear compression following release of calcium with TG in MCF10A (left column) and MCF10A co-expressing ∆50LaminA (right column). (**b**) Mean YAP N/C (normalized to initial time point) for MCF10A cells (N=137 tracks) and MCF10A cells co-expressing ∆50LaminA (N=106 tracks) upon treatment with TG. (**c**) Normalized projected nuclear area for MCF10A cells (N=166 tracks), and MCF10A cells co-expressing ∆50LaminA (N=87 tracks) upon treatment with TG.

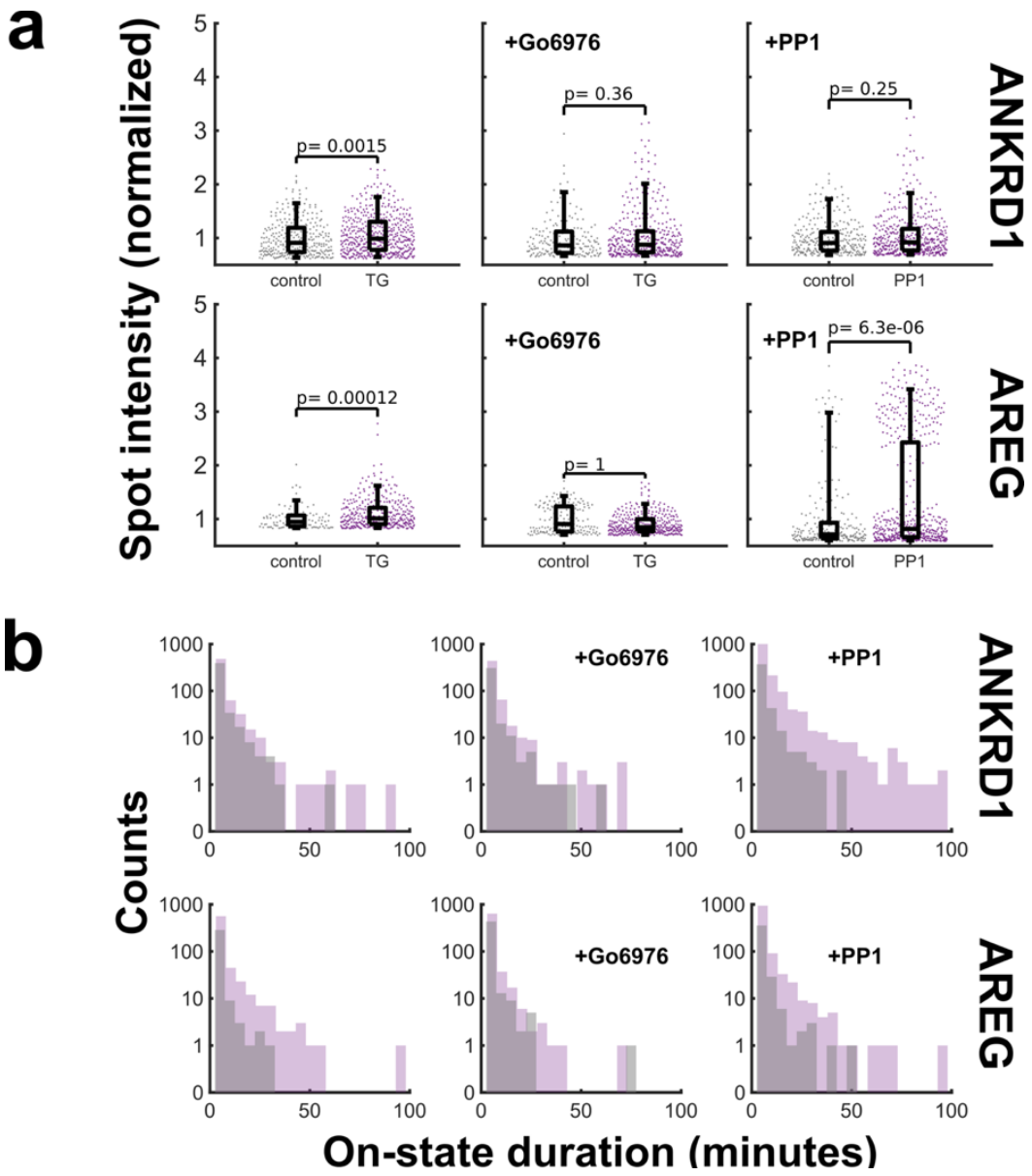

Supplementary Figure 4: Amplitude and duration analysis of AREG and ANKRD1 gene transcription pulses under various conditions. (**a**) Pulse amplitude comparison between pre-treatment period ('control') and post-treatment period ("TG" or "PP1"). For each individual experiment, the transcription amplitude was normalized to the pre-treatment period such that the mean intensity is 1. The one-sided Mann-Whitney U-test P-value is reported for each pre-treatment: post-treatment comparison. The distribution was generated by compiling data from all experiments. (**b**) The distribution of pulse-durations are shown for each pre-treatment: post-treatment comparison, as in **a**.

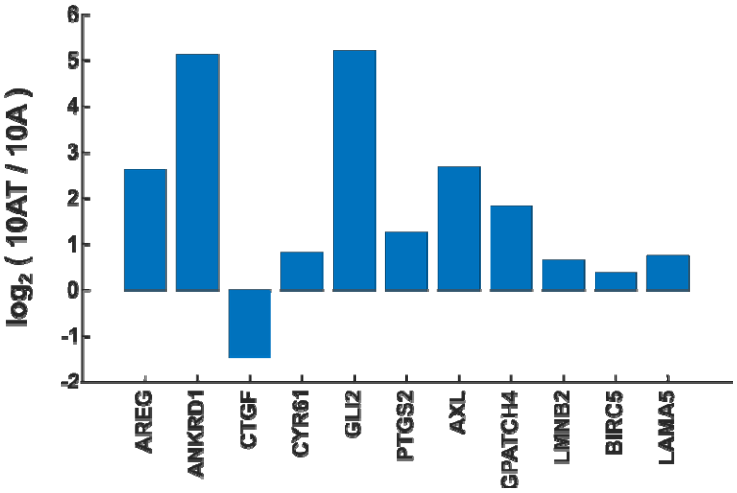

Supplementary Figure 5: Transformed mammary epithelial cells exhibit higher expression of YAP target gene. Gene expression in Ras-transformed MCF10A (10AT) relative to MCF10A (10A) for genes known to be regulated by YAP activity based on reported RNA-seq measurements (See Methods)**.**

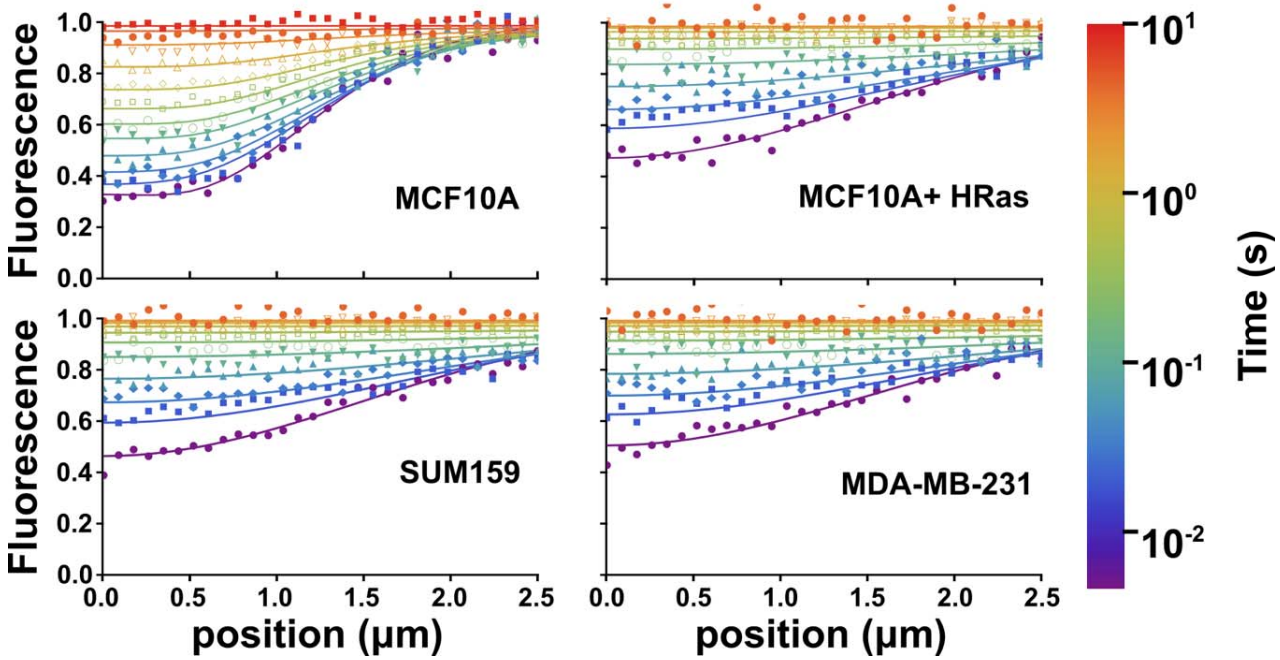

Supplementary Figure 6: Line FRAP reveals binding kinetics of YAP in normal and transformed breast epithelial cell lines. A spatio-temporal FRAP model was used to fit high-resolution line FRAP experiments of YAP in MCF10A (N=30 cells), MCF10A+HRas (N=26 cells), SUM159 (N=30 cells), and MDA-MB-231 (N=30). Markers represent the measured mean fluorescence values as a function of time (color bar) and position from bleach center (x-axis). The model fit is shown in solid colored lines.

Supplementary Table 1: Line-FRAP model fitting. Fitted model parameter values for MCF10A, MCF10A + HRas, SUM159, MDA-MB-231 for either a pure diffusion model or diffusion plus binding. Unrealistic values are highlighted in red. SSD is the sum of squared residuals between experiment data and model fit.

	diffusion		reaction-diffusion				
cell line	**D ($\mu m^2/s$)**	**SSD**	**D_{eff} ($\mu m^2/s$)**	**k_{on} (1/s)**	**k_{off} (1/s)**	**% Bound**	**SSD**
MCF10A	2.05±0.18	8.82±0.65	9.8±2.4	1.19±0.41	1.06±0.19	52±5	7.97±0.59
MCF10A+HRas	23.5±4.1	6.51±0.74	38.3±10.2	0.26±0.26	1.12±0.52	16±7	6.23±0.68
SUM159	26.8±5.1	2.57±0.40	40.8±10.9	0.66±1.03	3.34±5.1	15±6	2.46±0.40
MDA-MB-231	26.5±7.7	3.56±0.44	45.5±10.6	0.52±0.47	1.99±1.2	19±7	3.41±0.42

Supplementary Movies List

Supplementary Movie 1: YAP localization vs. density in MCF10A$^{YAP\text{-}GFP\text{-}KI}$ and HRas transformed MCF10A$^{YAP\text{-}GFP\text{-}KI}$

Supplementary Movie 2: Highlighted cell with rapid changes of YAP localization.

Supplementary Movie 3: YAP N/C localization in MCF10A$^{YAP\text{-}GFP\text{-}KI}$ cells, MCF10AT$^{YAP\text{-}GFP\text{-}KI}$ cells and MCF10A$^{YAP\text{-}GFP\text{-}KI}$ cells treated with the SRC inhibitor PP1.

Supplementary Movie 4: Coordinated fluctuation in YAP N/C in neighboring cells.

Supplementary Movie 5: YAP localization dynamics at wound edge.

Supplementary Movie 6: TG induced YAP localization in MCF10A control, Go6976 pre-treatment, and ∆50LaminA overexpression. TG added before frame 1.

Supplementary Movie 7: TG induced nuclear-deformation comparison between control and ∆50LaminA expressing cells.

Supplementary Movie 8: Tracking transcription kinetics before and after TG treatment in MCF10A$^{ANKRD1\text{-}MS2\text{-}KI}$ and MCF10A$^{AREG\text{-}MS2\text{-}KI}$ cells.

Supplementary Movie 9: Transcription kinetics before and after mitosis in MCF10A$^{ANKRD1\text{-}MS2\text{-}KI}$ and MCF10A$^{AREG\text{-}MS2\text{-}KI}$ cells. Time stamp is with respect to cytokinesis.